Construction and Building Materials 37 (2012) 111–124

Contents lists available at SciVerse ScienceDirect

Construction and Building Materials

journal homepage: www.elsevier.com/locate/conbuildmat

A simple approach to model SFRC

Bibiana Luccioni [a,*], Gonzalo Ruano [a], Facundo Isla [a], Raúl Zerbino [b], Graciela Giaccio [c]

[a] Structures Institute, National University of Tucumán, CONICET, Av. Independencia 1800, 4000 S.M. de Tucumán, Argentina[1]
[b] Civil Eng. Dept., National University of La Plata, CONICET, 47 y 115, 1900 La Plata, Argentina
[c] Civil Eng. Dept., National University of La Plata, Researcher CIC-LEMIT, 52 entre 121 y 122, 1900 La Plata, Argentina

HIGHLIGHTS

- A homogenization approach for Steel Fiber Reinforced Concrete (SFRC) is proposed.
- It presents advantages in comparison with equivalent isotropic homogeneous models.
- The model takes information from the micro-scale to model the macro-scale.
- Fiber content, distribution and pull out response are explicitly taken into account.
- Flexure response of SFRC beams with variable fiber content is properly modeled.

ARTICLE INFO

Article history:
Received 19 July 2011
Received in revised form 18 June 2012
Accepted 22 July 2012

Keywords:
Steel Fiber Reinforced Concrete
Self compacting concrete
Pull-out
Flexure
Numerical model
Composite

ABSTRACT

Experimental research that shows the improvement in structural behavior of concrete with the addition of fibers has been developed in the last years. Fibers control cracking and thus increase concrete toughness and ductility. Much effort has been devoted in the last decade to model this material.

A simple homogenization approach based on a modified mixture theory is proposed in this paper to model Steel Fiber Reinforced Concrete (SFRC). The proposed and calibrated model takes information from the micro-scale to model the macro-scale. SFRC is considered as a composite material composed by concrete matrix and fibers. Concrete is modeled with an elastoplastic model and steel fibers are considered as orthotropic elastoplastic inclusions that can debond and slip from the matrix. In order to include this inelastic phenomenon without explicitly modeling interface, constitutive equations of fibers are modified including information from the debonding–slipping phenomena. The model requires concrete properties, fibers material, geometry, distribution and orientation as input data. The fibers bond–slip behavior is automatically derived from concrete properties and fibers geometry or it can be alternatively obtained from pull out tests.

As illustration, the tension response of SFRC with different fiber contents is numerically simulated. The model is verified with the results of bending tests of beams extracted from a SFRC slab that present different fibers distribution due to the slab casting process. Comparisons with other numerical approaches modeling SFRC as an equivalent homogeneous material are also included in the paper.

1. Introduction

A high performance material is obtained when fibers are introduced in concrete. Many works have shown the advantages of using Steel Fiber Reinforced Concrete (SFRC) in applications that mainly include tunnel linings, pavements, shotcretes, overlays and repairs. Fibers contribute to the control of crack propagation and enhance mechanical properties, improving bond, fatigue and impact performance. Significant progress has been achieved more recently. New fibers were produced including synthetic fibers, criteria for mechanical characterization and structural design were proposed, and it was demonstrated that fibers can be used in high fluidity mixtures as self compacting concrete.

It is recognized that the casting and compaction processes may affect fiber orientation in the structural elements. In the case of Fiber Reinforced Self Compacting Concrete, significant changes in orientation produced by concrete flow and proximity to molds walls were observed [1–3]. As in conventional vibrated SFRC, a 2D orientation appears in self-compacting SFRC [4]. Fibers align along the flow of fresh concrete but after certain distance the fiber alignment is not important [3]. The changes in distribution and orientation of the reinforcement leads to important differences in post peak behavior.

* Corresponding author.
E-mail address: bluccioni@herrera.unt.edu.ar.edu.ar (B. Luccioni).
[1] www.herrera.unt.edu.ar/iest.

0950-0618/$ - see front matter © 2012 Elsevier Ltd. All rights reserved.
http://dx.doi.org/10.1016/j.conbuildmat.2012.07.027

Due to the well performance of SFRC in many structural and non-structural applications much effort has been devoted in the last decade to model this material [5]. As in the case of all fiber reinforced composite materials, different approaches can be used to simulate SFRC non-linear behavior.

Constitutive models for SFRC can be classified in macro-models and micro-models according to the scale in which they are defined.

In macro-models the composite material is represented as a unique material with average properties. These types of models are usually based on a phenomenological approach in which the constitutive laws are obtained from laboratory tests.

In some recent papers, models originally developed for plain concrete are modified to simulate the behavior of SFRC. These models are based on different approaches for the continuum like microplane model [6], smeared crack models [7], discrete crack models, elastoplastic models like Willam–Warnke model [8], damage models [9,10] or non-linear models calibrated with experimental results from tension and compression tests [11]. Constitutive models available for concrete in commercial hydrocodes are calibrated with experimental results from SFRC tests to reproduce impact response of this material in some recent papers [12,13].

The main task in this type of approach is the definition of the tensile behavior of SFRC that can be measured in direct tension tests or indirectly obtained through an inverse analysis from bending tests results [14].

The advantage of this phenomenological approach is the use of material information at the relevant scale for the analysis of the structure [5]. The main drawback is the need of extensive and costly experimental tests [5]. Since micromechanical behavior is not explicitly modeled, fiber volume fraction, aspect ratio, type, distribution and orientation cannot be taken into account and experimental results should be obtained every time each of this data influencing SFRC behavior is changed.

Moreover, the selection of the $\sigma - w$ to be used in tension is not a simple task. Curves obtained from direct tension tests are not reliable because a great variability is usually obtained. Belletti et al. [15] pointed out that $\sigma - w$ or $\sigma - \varepsilon$ indirectly obtained from notched beam bending tests can be affected by the crack model used, mesh size, element integration scheme and analytical model.

Many of these problems can be avoided with micromechanical derived models. The development of constitutive models relating the micro-structural parameters to the mechanical behavior of fiber composites is also motivated by the possibility of designing the material for each application and predicting the behavior of the designed material [16].

Constitutive relations micromechanically derived involve two major steps: (1) derivation of crack bridging force for a single fiber in terms of microparameters and (2) derivation of the composite behavior for a given fiber distribution [17]. Models differ in the way in which these two steps are developed. The derivation of the crack bridging forces can be done from experimental pull out tests or micromechanically derived. Additionally, SFRC behavior can be obtained through homogenization techniques from the properties of its constituents (concrete and fibers) and the shape, volume fraction, orientation and distribution of fibers or alternative fibers can be explicitly modeled using different types of discrete elements.

A statistical micromechanical model of the tension-softening behavior of short fiber-reinforced composites based on the random nature of fiber distribution and accounting for dominant features of the composite failure mechanisms like fibers pulled out at an angle to the matrix crack plane as well as slip-weakening or hardening of the fiber interface during the pull-out process, was presented by Li et al. [16].

Based on fiber pullout curves derived from a micromechanical model, Leung and Geng [18] established the tensile stress–displacement relation along a Mode I (opening) and used a statistical model to account for random fiber distribution. The composite behavior was simulated with a finite element code using a discrete crack approach and placing truss elements across the crack to simulate the fiber bridging effect [18]. Lange-Kornbak and Karihaloo [19] developed a model for the tension softening response of short-fiber-reinforced cementitious composites in which the cracks in the localization zone are bridged along their entire length by adhesively or frictionally bonded fibers.

Li and Li [20] developed a continuum damage approach to model SFRC in tension. They proposed a parallel bar model in which fibers and concrete were connected by parallel-series components. Two damage variables related to matrix and fibers were defined. The fiber–matrix interface properties were explicitly taken into account in the model.

A constitutive model for cohesive fracture of fiber reinforced concrete was proposed by Park et al. [21] by differentiating the aggregate bridging zone and the fiber bridging zone. The cohesive fracture model is defined by experimental fracture parameters, which are obtained through three-point bending and split tensile tests.

Pasa Dutra et al. [5] developed a homogeneization method for the elastic and viscoelastic behaviors of SFRC. They assumed a matrix/inclusion morphology for SFRC. The fibers were modeled as flat spheroids, and a Mori–Tanaka homogenization scheme was used to estimate the overall elastic properties. The model assumed no slip on the matrix–fiber interface.

Recently, Gal and Kryvoruk [22] proposed a two-step homogenization approach to evaluate elastic properties of SFRC. The suggested framework executes the multi-scale analysis of SFRC structures by incorporating an original concrete unit cell generator into a commercial finite element software package.

Alternatively, some approaches that consider the discrete contribution of fibers in SFRC were proposed. Bolander [23] models individual fibers and fiber–matrix interface, within a random lattice representation of the material matrix. Radtke et al. [24] represent concrete with a regularized damage model and model it with the finite element method. Fibers are treated as discrete entities which are not related to the matrix discretization but represented by reaction forces. These forces take into account fiber action and fiber–matrix interface and contain information from the micro-scale obtained from pull-out relations. Cunha et al. [25] use a smeared crack model for concrete and assume steel fibers as embedded short cables distributed within matrix according to a Monte Carlo method. The stress–slip relations for the fibers are obtained from pull-out tests.

A simple homogenization approach for SFRC based on a modified mixture theory is proposed in this paper. The proposed and calibrated model takes information from the micro-scale to model the macro-scale. SFRC is considered as a composite material composed by concrete matrix which is modeled with an elastoplastic model [26,27] and steel fibers are considered as orthotropic elastoplastic inclusions that can debond and slip from the matrix. Constitutive equations of fibers are modified using the approach proposed by Luccioni et al. [28] in order to include this inelastic phenomenon without explicitly modeling the interface. The model requires concrete properties, fibers material, geometry, distribution and orientation as input data. The fibers bond–slip behavior is automatically derived following the ideas originally proposed by Naaman et al. [29–31] and Chanvillard [32] or it can be alternatively obtained from pull out tests.

The model is calibrated with experimental results from concrete compression tests and fibers pull out tests and verified with the results of bending tests of beams extracted from a self compacting SFRC slab. The beams show significant differences in fibers orientation and distribution when different zones or directions

(normal or parallel to flow) of the slab are considered. Consequently, the load–crack opening displacement curves are different. Many of these curves are properly reproduced proving the ability of the proposed model to simulate the response of SFRC with different fibers contents and distributions.

2. Composite model

SFRC can be regarded as composite material formed by a brittle concrete matrix with short disperse fibers that can debond and slip from the matrix. Fibers are usually not randomly distributed but follow some preferment alignment related to the casting process and the mold walls.

One of the simplest ways of modeling composites behavior using information from the microscale is the mixture theory. This theory is based on strong simplifying assumptions and cannot be directly applied to the simulation of a composite material with the characteristics described. Nevertheless, there are some previous papers showing that the original mixture theory can be successfully modified to reproduce fibers anisotropy, debonding and slipping [28,33,34].

The theory of mixtures is based on the following assumptions [35]:

(1) the set of component substances is present in each infinitesimal volume of the composite;
(2) each component contributes to the behavior of the composite in proportion to its volumetric participation;
(3) the volume occupied by each component is lesser than the volume occupied by the composite; and
(4) all the components have the same strain (compatibility condition). For small strains, and two component composite materials this last assumption is written

$$\varepsilon_{ij} = (\varepsilon_{ij})_m = (\varepsilon_{ij})_f \tag{1}$$

where the sub indexes m and f refer to concrete matrix and steel fibers respectively. The strain compatibility assumption constitutes a strong limitation of the mixtures theory. In particular, fiber slipping represents a strong discontinuity in the strain field inside the composite that cannot be simulated with this theory. When debonding occurs, the stress transfer between the matrix and the fibers through the fiber–matrix interface is affected and a stress reduction results in the fibers. This stress reduction can be assimilated to a strain reduction related to the interface deformation [28]. The strain compatibility Eq. (1) can be replaced by the following equation,

$$(\varepsilon_{ij})_f = \varepsilon_{ij} - (\varepsilon_{ij})_s = (\varepsilon_{ij})_m - (\varepsilon_{ij})_s \tag{2}$$

where strain tensor $(\varepsilon_{ij})_s$ represents a measure of the interface deformation or slipping. This deformation depends on the stress state and is composed of an elastic component and an irrecoverable component. In general, the elastic component can be neglected when compared with the inelastic deformation, the latter being interpreted as an irrecoverable deformation which takes place as a result of the fiber debonding–slipping.

If an elastoplastic behavior is assumed for steel, the fiber's secant constitutive equation can be written as follows,

$$(\varepsilon_{ij})_f = (C_{ijkl})_f[(\varepsilon_{kl})_f - (\varepsilon^p_{kl})_f] = (C_{ijkl})_f[\varepsilon_{kl} - (\varepsilon_{kl})_s - (\varepsilon^p_{kl})_f] \tag{3}$$

where $(\varepsilon^p_{ij})_f$ represents the fiber permanent strains and $(C_{ijkl})_f$ is the fibers secant constitutive tensor.

Eq. (3) can be interpreted as describing two dissipative mechanisms that simultaneously take place in the set formed by the steel fibers together with the fiber–matrix interface. One dissipative mechanism is due to steel inelastic strains and the other is due to debonding and slipping of the steel fibers.

On the other hand, the composite free energy density can be written [35]

$$\Psi(\varepsilon_{ij}, \alpha_i) = k_m \Psi_m(\varepsilon_{ij}, p_{mi}) + k_f \Psi_f((\varepsilon_{ij})_f, p_{f_i}, s_i) \tag{4}$$

where Ψ_m and Ψ_s are the free energy density of matrix and fibers respectively, $k_m = \frac{dV_m}{dV}$ and $k_f = \frac{dV_f}{dV}$ are the corresponding volume ratios; p_{mi}, p_{f_i} and s_i represent sets of internal variables associated with dissipative processes taking place in matrix, fibers and fiber/matrix interface respectively.

The composite secant constitutive equation can be obtained from Coleman relations that guarantee the fulfillment of Clasius Duhem inequality,

$$\begin{aligned} \sigma_{ij} &= \frac{\partial \Psi(\varepsilon_{kl}, \alpha_k)}{\partial \varepsilon_{ij}} = k_m \frac{\partial \Psi_m(\varepsilon_{ij}, p_{mi})}{\partial \varepsilon_{ij}} + k_f \frac{\partial \Psi_f((\varepsilon_{ij})_f, p_{f_i}, s_i)}{\partial \varepsilon_{ij}} \\ \sigma_{ij} &= k_m(\sigma_{ij})_m + k_f(\sigma_{ij})_f \end{aligned} \tag{5}$$

where the stresses $(\sigma_{ij})_m$ and $(\sigma_{ij})_f$ are obtained from the matrix and the fiber constitutive equations respectively.

An elastoplastic damage model is used for concrete while an anisotropic elastoplastic model including debonding–slipping is used for the fibers.

2.1. Concrete constitutive model

A modified plastic model is used for concrete [27]. The plastic behavior is obtained as a generalization of classical theory of plasticity especially appropriate for geomaterials.

The elastic behavior limit is defined through a yield function:

$$F(\sigma_{ij}; \kappa^p) = f(\sigma_{ij}) - \mathrm{K}(\sigma_{ij}; \kappa^p) \leqslant 0 \tag{6}$$

where $f(\sigma_{ij})$ is the equivalent stress. A modified Lubliner–Oller yielding criterion is used in this paper [27]. $K(\sigma_{ij}; \kappa^p)$ is the yield threshold and κ^p is the plastic damage variable or isotropic plastic hardening variable.

The following flaw rule is defined for the plastic strains.

$$\dot{\varepsilon}^p_{ij} = \dot{\lambda} \frac{\partial G(\sigma_{mn}; \alpha_k)}{\partial \sigma_{ij}} \tag{7}$$

where $\dot{\lambda}$ is the plastic consistency parameter and G is the plastic potential function.

The plastic hardening variable κ^p is obtained normalizing energy plastically dissipated to unity and varies between 0 for the virgin material and 1 when the material has dissipated all the available energy. The evolution law for the plastic hardening variable takes into account the differentiated behavior in tension and compression and properly simulates energy dissipation for triaxial compression processes:

$$\dot{\kappa}^p = \left[\frac{r}{g^{*p}_f} + \frac{(1-r)}{g^{*p}_c}\right] \sigma_{ij} \dot{\varepsilon}^p_{ij} \tag{8}$$

where

$$r = \frac{\sum_{i=1}^{3} \langle \sigma_i \rangle}{\sum_{i=1}^{3} |\sigma_i|} \quad \langle \sigma_i \rangle = \frac{1}{2}[\sigma_i + |\sigma_i|] \tag{9}$$

σ_i are the principal stresses

$$g^{*p}_f = \left(\frac{\sum_{i=1}^{3} |\sigma_i| \mathrm{R}^{op}}{f^p(\sigma_{ij})}\right)^{1+H(-r)} g^p_f \quad g^{*p}_c = \left(\frac{\sum_{i=1}^{3} |\sigma_i|}{f^p(\sigma_{ij})}\right)^{1+H(-r)} g^p_c \tag{10}$$

$$H(-x)\begin{cases} = 0 \text{ if } x > 0 \\ = 1 \text{ if } x \leqslant 0 \end{cases}$$

R^{op} is the compression/tension yield threshold ratio, g_f^p and g_c^p are the maximum energy densities dissipated in uniaxial tension and compression respectively and can be evaluated as follows

$$g_f^p = \frac{G_f}{l_c} \quad \text{and} \quad g_c^p = \frac{G_c}{l_c} \tag{11}$$

where G_f and G_c are fracture and crushing energies respectively and l_c is an externally parameter that depends on the finite element mesh introduced to achieve response objectivity respect to the finite element mesh size.

The following evolution law is used for the equivalent yielding threshold.

$$K(\sigma_{ij}, \kappa^p) = r\sigma_t(\kappa^p) + (1-r)\sigma_c(\kappa^p) \tag{12}$$

where $\sigma_t(\kappa^p)$ and $\sigma_c(\kappa^p)$ represent the yielding thresholds evolution in uniaxial tension and compression tests respectively.

Loading/unloading conditions are derived from the Kuhn-Tucker relations formulated for problems with unilateral restrictions.

$$\dot{\lambda} \geqslant 0 \quad F^p \leqslant 0 \quad \dot{\lambda}F^p = 0 \tag{13}$$

2.2. Constitutive model for fibers

As pointed out in Eq. (3) two dissipative mechanisms take place in the set of fiber and fiber/matrix interface. Associated with these mechanisms, two sets of internal variables may be defined. The following flow rules are used for the inelastic strains of the fibers and the debonding–slipping deformations [28]:

$$(\dot{\varepsilon}_{ij}^p)_f = \dot{\lambda}_p \frac{\partial G_p}{\partial(\sigma_{ij})_f}; \quad \dot{p}_i = \dot{\lambda}_p h_i^p \tag{14}$$

$$\dot{\lambda}_p \begin{cases} = 0 \text{ if } F_p((\sigma_{ij})_f, p_i) < 0 \\ > 0 \text{ if } F_p((\sigma_{ij})_f, p_i) = 0 \end{cases} \tag{15}$$

$$(\dot{\varepsilon}_{ij}^s)_f = \dot{\lambda}_s \frac{\partial G_s}{\partial(\sigma_{ij})_f}; \quad \dot{s}_i = \dot{\lambda}_s h_i^s \tag{16}$$

$$\dot{\lambda}_s \begin{cases} = 0 \text{ if } F_s((\sigma_{ij})_f, s_i) < 0 \\ > 0 \text{ if } F_s((\sigma_{ij})_f, s_i) = 0 \end{cases} \tag{17}$$

where p_i and s_i represent sets of internal variables associated with plasticity and slipping mechanisms and h_i^p and h_i^s are tensors defining the flow of each of the internal variables. G_p and G_s represent convex potential functions; $\dot{\lambda}_p$ and $\dot{\lambda}_s$ are plastic and slipping consistency parameters; and F_p and F_s plasticity and slipping threshold functions, respectively, which should also be convex functions [36].

The way in which fibers plastic orthotropy is taken into account in Eqs. (14) and (15) is first presented in Section 2.2.1. Then the model used to simulate fiber debonding–slipping phenomenon in Eqs. (16) and (17) is described in Section 2.2.2.

2.2.1. Plastic orthotropy

It is well known that, although steel can be considered isotropic itself due to their geometry steel fibers present a marked orthotropy characterized not only by the elastic orthotropy but also by the marked difference of strength and debonding strength in the principal directions.

The approach used in this paper to handle orthotropy is based on the assumption that two spaces can be defined [37,38]: (a) a real anisotropic space and (b) a fictitious isotropic space. The problem is solved in the fictitious isotropic space allowing the use of elastoplastic models originally developed for isotropic materials.

Stress tensors in both spaces are related by a tensor transformation that can be written as,

$$\tau_{ij} = A_{ijkl}(\sigma_{ij}, \kappa^p)\sigma_{kl} \tag{18}$$

where τ_{ij} and σ_{kl} are the stress tensors in spaces (a) and (b) respectively, and A_{ijkl} is a fourth order transformation tensor that contains the information about strength anisotropy depending on material symmetry. In the most general case, this tensor varies with the stress state and the evolution of the inelastic process represented by the isotropic plastic hardening variable κ^p. In this paper, fibers are assumed initially orthotropic with three axes of material symmetry. There are different alternatives to define tensor A_{ijkl} for this case [39–41]. The simplest way is a diagonal fourth order tensor [34],

$$A_{ijkl} = \sum_{m=1}^{3}\sum_{n=1}^{3} \delta_{im}\delta_{jn}\delta_{km}\delta_{\ln}\bar{\tau}/\bar{\sigma}_{mn} \tag{19}$$

where $\bar{\tau}$ is the strength in the fictitious isotropic space and $\bar{\sigma}_{mn}$ is the actual strength in the direction m in the plane with normal n. A better approach has been proposed by Oller et al. [41].

The plastic threshold is defined through a yielding function,

$$F_p(\sigma_{ij}; \kappa^p) = \overline{F}_p(\tau_{ij}; \bar{\kappa}^p) = 0 \tag{20}$$

where F and $\overline{F}$ represent the yielding function in the real anisotropic space and the fictitious isotropic space respectively; κ^p and $\bar{\kappa}^p$ are plastic internal variables in correspondence with both spaces.

The transformation defined by Eq. (18) allows the use of yielding functions $\overline{F}$ defined for isotropic materials in the fictitious isotropic space. It should be noted that this space is isotropic with respect to yielding thresholds and strength but not necessarily with respect to other properties like elastic stiffness.

This concept can be extended to the case of plastic flaw rule too. Instead of working with potential functions that should be anisotropic, function $\overline{G}_p$ defined in the fictitious isotropic space could be used.

$$G_p(\sigma_{ij}; \kappa^p) = \overline{G}_p(\tau_{ij}; \bar{\kappa}^p) \tag{21}$$

Eq. (14) can then be rewritten as,

$$\dot{\varepsilon}_{ij}^p = \dot{\lambda}(\partial\overline{G}_p/\partial\sigma_{ij}) = \dot{\lambda}(\partial\overline{G}_p/\partial\tau_{kl})(\partial\tau_{kl}/\partial\sigma_{ij}) = \dot{\lambda}(\partial\overline{G}_p/\partial\tau_{kl})A_{klij} = \dot{\lambda}h_{ij} \tag{22}$$

where $\partial\overline{G}_p/\partial\tau_{kl}$ is a second-rank tensor and represents the plastic flow in the fictitious isotropic space.

2.2.2. Fiber debonding–slipping model

Fibers matrix bonding has several components: physical and/or chemical adhesion, frictional strength and a mechanical component associated with the fiber geometry that acts as an anchorage. In most cases, fibers are pulled out from the matrix once they have lost their adherence to it and before they reach rupture. Therefore, the longer the fibers the greater their capacity to resist pull-out forces. This phenomenon is normally studied through experimental tests called pull-out tests [29–32,42–49].

For the case of straight fibers immersed in concrete the basic components contributing to pull-out strength are adhesion and friction. When an axial force is applied to the fiber, adhesion initially acts on the total length of the fiber. Shear stresses in the fiber–matrix interface are not uniform and the maximum stresses are located near the crack. If the axial force is increased beyond the adhesion strength, the fiber begins to debond from the matrix and friction starts to act in these zones. When the complete interface has lost adhesion, slipping is initiated with a marked drop in pull-out strength that is only provided by friction. As the fiber is pulled out, friction decreases due to a combined action of abrasion and cement and sand particles compaction around the fiber. This is the case of straight fibers. To prevent the sharp drop of pull-out strength when adhesion has run through, fibers with special

geometry, as fibers with hooks at their ends or wavy fibers or fibers with polygonal cross section are used. In this way a mechanical component is added to pull-out strength.

Pull-out strength also depends on matrix integrity. If the matrix is progressively disintegrated as the fiber is pulled out, all the resistant capacity and ductility of the fibers cannot be exploited. For this reason, some authors have tried to combine fibers of different sizes where the shorter fibers are responsible of preserving the stability of the matrix while the longer fibers bridge the cracks developing the maximum capacity of the later [50].

A debonding–sliping criterion, a flow rule and a hardening rule should be specified in Eqs. (16) and (17) in order to complete the SFRC model previously defined. In this case in which fibers are assumed as component materials in mixture theory the debonding–slipping criteria is mainly a limit in fibers axial stress and slipping is assumed to be in the direction of the fibers so the flow vector $\frac{\partial G_s}{\partial \sigma_{ij}}$ is known in advance and is constant.

The fibers pull-out curve can be used in order to define the debonding–slipping criteria and the hardening/softening law. The load–displacement curves obtained from the tests have different shapes mainly depending on the number of curve parts, the length of the different fiber parts and their curvature ratio, that is, on the fiber axis geometry. The final shape and the pull-out strength also depend on the fiber diameter, its surface texture and the mortar quality.

The pull-out curve can be obtained from pull-out tests or alternative it can be numerically simulated modeling the debonding–slipping process. Both approaches were used and compared in this paper and are presented in the following sections.

A different simplified alternative consists of the estimation of the fibers pull-out response from flexure tests. This approach is an inverse method requiring the calibration of a very simplified, bilinear o three-linear pull-out curve from the numerical simulation of flexure tests. This approach is also used in this paper and the results are shown together with flexure tests numerical results.

The numerical model used for fiber pull-out simulation [51] is based on the models originally developed by Naaman et al. [29,52] (model for straight fibers) and Chanvillard [32] (model for curve axis fibers).

The analysis consists of two steps, the first step simulates the elastoplastic process in the interface and the loss of adhesion between fiber and matrix (crack that surrounds the fiber and propagates through the interface, up till the slip beginning) [52]. See Fig. 1

The second step comprises the fiber slipping process [32] once all the adhesion has been exhausted. The fiber axial deformation is assumed negligible and the pull-out strength is supposed to be the result of friction and fiber curvature change. See Fig. 2. Friction is assumed to be provided by:

- Fiber surface irregularities due to the manufacturing process and to the shape change and from the wedging of the material released from the matrix during the fiber slipping.
- Changes of fiber axis curvatures. The change of direction of the axial force implies a normal force that compresses the concave part of the fiber against the matrix.
- Lateral confinement of the fiber provided by the matrix under a multiaxial stress state.

The fiber axial stress σ_f that should be transmitted through the interface can be estimated as follows,

$$\sigma_f = \frac{1}{A_f}\int_0^L \left(\frac{dC(s)}{d\delta}M + \tau_d\psi + P(s)C(s)r - \tilde{\sigma}\psi r\right)ds \tag{23}$$

where A_f is the fiber cross sectional area, s the curvilinear coordinate along the fiber axis, ψ the fiber perimeter, L the fiber length in contact with the matrix, $C(s)$ the fiber curvature in position s, δ the fiber slipping, M the moment developed by the fiber change of curvature, τ_d the friction stress, r the friction coefficient, $\tilde{\sigma}$ the mean confinement stress resulting from the matrix action on the fiber, $P(s)$ is the pull-out strength provided from the fiber end to the position s

2.3. Numerical implementation

The material models used for the different approaches presented in this paper were implemented in 3D and 2D non-linear finite element programs developed for research purposes. Nevertheless, they can be easily introduced as user subroutines in commercial codes.

In the code used in this paper the material is supposed to be formed by several components. When using the equivalent homogeneous approach, only one component is assumed for SFRC.

A Newton Raphson algorithm is used for the iterative solution of global equilibrium equations. The strain tensor is known for each iteration. According to classical mixture theory, all the components have the same strain (see Eq. (1)) and therefore, the constitutive equations can be separately integrated to obtained the stress tensors of each of the components that can be combined using Eq. (5) to get the composite stress. The described procedure is sketched in Fig. 3 where $\boldsymbol{U}$ is the nodal displacement vector, $\Delta\boldsymbol{U}$ is the nodal displacement increment, $\boldsymbol{K}$ is the stiffness matrix and $\boldsymbol{F}_{resid} = \boldsymbol{F}_{ext} - \boldsymbol{F}_{int}$is the residual force vector.

The elastoplastic models defined for the components are integrated using a return mapping [53] algorithm. In the case of the fibers the plastic and slipping constitutive equations are simultaneously integrated.

The plastic and slipping consistency conditions in load step n, iteration k, are posed as a linearization around iteration $k-1$.

$$[F_p]_n^k = [F_p]_n^{k-1} + \left[\frac{\partial F_p}{\partial \sigma_{ij}}\right]_n^{k-1}\delta\sigma_{ij}^k + \left[\frac{\partial F_p}{\partial p_i}\right]_n^{k-1}\delta p_i^k = 0 \tag{24}$$

$$[F_s]_n^k = [F_s]_n^{k-1} + \left[\frac{\partial F_s}{\partial \sigma_{ij}}\right]_n^{k-1}\delta\sigma_{ij}^k + \left[\frac{\partial F_s}{\partial s_i}f\right]_n^{k-1}\delta s_i^k = 0$$

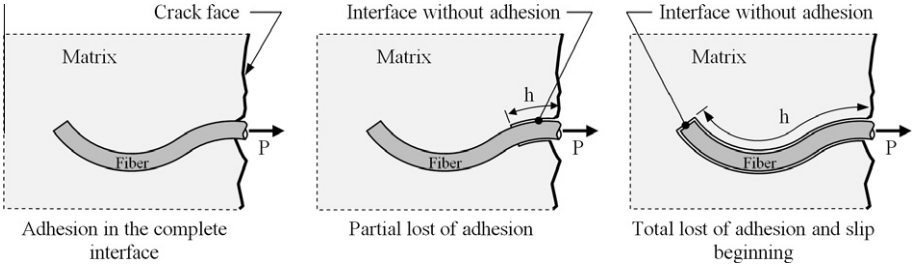

Fig. 1. Adhesion lost before slipping.

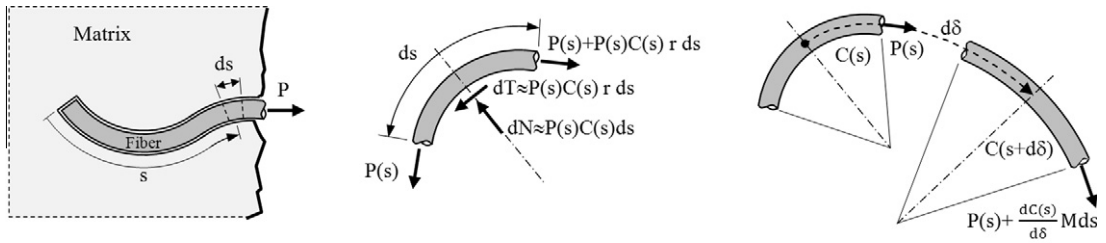

(a) Fiber-matrix interface without adhesion. Slipping beginning.

(b) Fiber deferential element. Friction due to the change of direction [32].

(c) Fiber deferential element. Friction due to the change of curvature [32].

Fig. 2. Fiber slipping. Friction components.

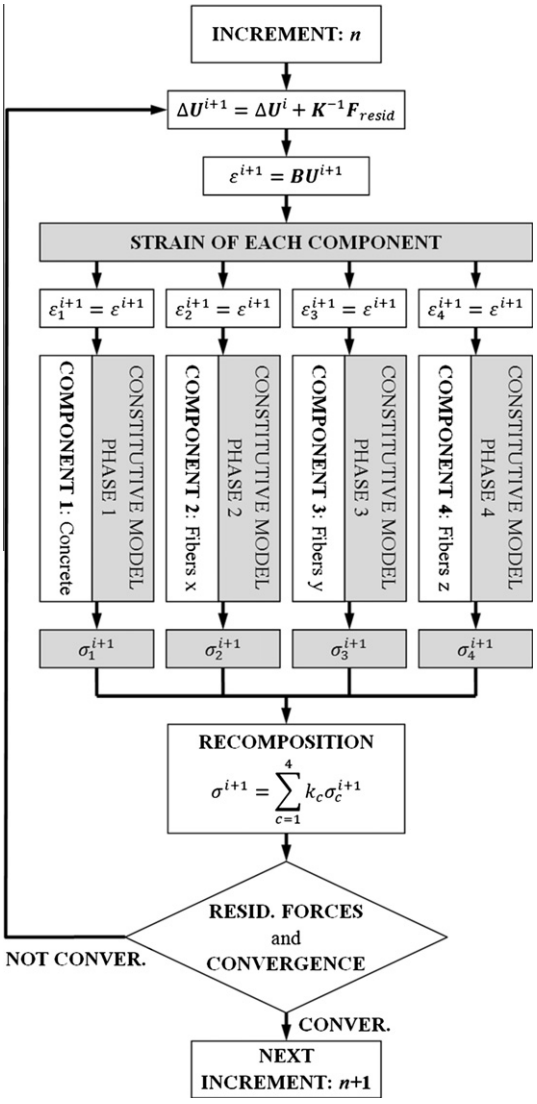

Fig. 3. Numerical integration of the composite model.

where

$$\delta\sigma_{ij}^{k} = C_{ijlm}\left(-\delta\lambda_p^k\left[\frac{\partial G_p}{\partial\sigma_{lm}}\right]_n^{k-1} - \delta\lambda_s^k\left[\frac{\partial G_s}{\partial\sigma_{lm}}\right]_n^{k-1}\right) \tag{25}$$

$$\delta p_i^k = \delta\lambda_p^k[h_i^p]_n^{k-1} \quad \delta s_i^k = \delta\lambda_s^k[h_i^s]_n^{k-1} \tag{26}$$

If Eqs. (25) and (26) are replaced in Eq. (24), linear system in $\delta\lambda_p$ and $\delta\lambda_s$ is obtained. Solving this system the variables can be updated as follows,

$$(\varepsilon_{ij}^p)_n^k = (\varepsilon_{ij}^p)_n^{k-1} + \delta\lambda_p^k\left[\frac{\partial G_p}{\partial\sigma_{ij}}\right]_n^{k-1} \qquad (\varepsilon_{ij}^s)_n^k = (\varepsilon_{ij}^s)_n^{k-1} + \delta\lambda_s^k\left[\frac{\partial G_s}{\partial\sigma_{ij}}\right]_n^{k-1} \tag{27}$$

$$p_i^k = p_i^{k-1} + \delta\lambda_p^k[h_i^p]_n^{k-1} \quad s_i^k = s_i^{k-1} + \delta\lambda_s^k[h_i^s]_n^{k-1} \tag{28}$$

$$(\sigma_{ij})_n^k = C_{ijlm}((\varepsilon_{ij})_n - (\varepsilon_{ij}^p)_n^k - (\varepsilon_{ij}^s)_n^k) \tag{29}$$

The same algorithm can be used for concrete but in this case only one dissipative process is activated. Thus, only the first of Eqs. (24), (26)–(28) are solved.

Whether the pull-out curve is obtained from pull-out tests or it is numerically simulated, it constitutes input data for the slipping model.

3. Experimental program

The experimental program includes pull-out tests performed on composed mortar–fiber specimens to analyze the bond slip mechanisms of steel fibers and to obtain the data for the model calibration.

In order to verify the model, a slab was molded with a self-compacting SFRC. The selection of this type of concrete and structural element makes possible the analysis of different postpeak behaviors as there is important concrete flow during casting. In this way, the effect of fiber orientation on the residual mechanical properties of concrete can be considered.

The experimental details and the obtained results are presented next.

3.1. Pull out tests

Pull-out tests were performed on 40 × 20 × 160 mm prisms with rectangular cross section and an interruption in the middle that separated them in two parts that are joined by a fiber in the center as shown in Fig. 4a. The matrix interruption simulates the crack and allows the evaluation of the fiber pull out resistance.

Fig. 4b shows the pull-out test setup. The specimens were tested under uniaxial tension with displacement control using a loading rate of 0.01 mm/s during the first 5 mm, then the loading rate was increased to 0.05 mm/s up to 10 mm and finally, a constant loading rate of 0.1 mm/s was applied until the fiber was completely pulled out.

A 60 MPa mortar and five types of hooked end fibers were used. See Table 1.

Four load–slippingt curves corresponding to Fiber 5 (Table 1) are presented in Fig. 5. These curves show a marked decay of the pull-out force in correspondence with the straightened of the fibers curve parts while slipping. This observation shows the important contribution of curve parts to pull out strength.

It is observed that in case of hooked end fibers, the pulled out end looks straight but with some imperfections after the test. These imperfections are located at fibers ends and thus maintain a constant friction during the slipping up to the complete pull out. In the case of straight fibers, friction decreases during the slipping due to a combined action of abrasion and compaction of the matrix around the fiber [29]. These phenomena of abrasion and compaction also take place in the case of hooked end fibers but, due to the imperfections, they do not have the same effect on friction.

The mean peak pull out load, displacement corresponding to peak load and residual load for a displacement of 10 mm are included in Table 1 for each type of hooked end fibers tested. The pull-out strength (peak pull-out force) increases with the fiber diameter and with strength of the fiber material. Nevertheless, it was observed in the tests that fibers with greater pull-out strength are more likely to slip from both ends. The fiber slenderness (L/Φ) and the peak pull-out force

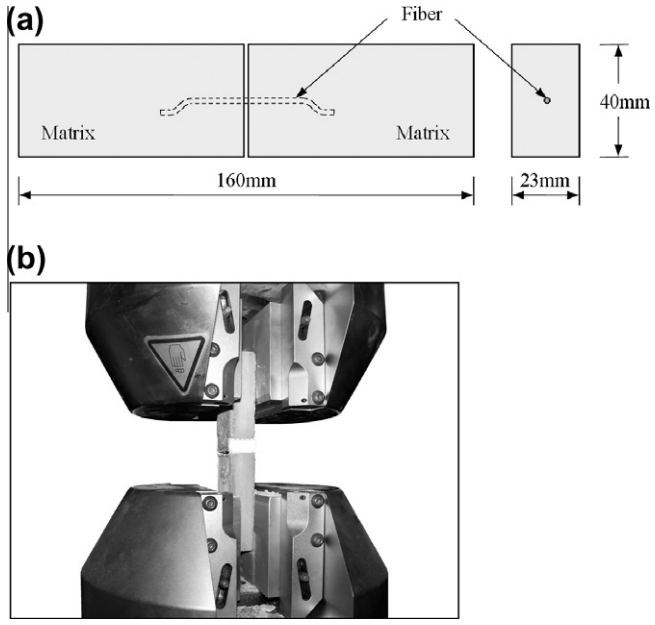

Fig. 4. Pull-out test. (a) Specimen dimensions, and (b) loading setup.

divided by the fiber volume ($V = \pi\Phi^2 L/4$) for the different fibers tested are also presented in Table 1. It is observed that, in general, more slender fibers give a greater pull-out strength for the same fiber volume ratio. This tendency is valid up to certain slenderness (L/Φ) from which pull-out strength begins to decrease. This observation is coincident with the effect of fibers slenderness on the behavior of SFRC reported by different authors [54].

3.2. Effect of fiber distribution and orientation on the behavior of SFRC

3.2.1. Self-compacting SFRC slab

A slab 0.9 × 1.8 × 0.09 m was cast with a self-compacting concrete incorporating 35 kg/m^3 of hooked end steel fibers 35 mm length and 0.45 mm diameter, aspect ratio of $L/\Phi = 77.7$ (Fiber 5 in Table 1). Concrete incorporated 640 kg/m^3 of normal portland cement + calcareous filler, natural siliceous sand, 12 mm maximum size granitic crushed stone and policarboxilated based superplasticizer. The main characteristics of this SFRC were: slump-flow = 700 mm, V-funnel time = 9.3 s and 28-days compression strength = 61.3 MPa.

Concrete was poured from one extreme of the slab. For the analysis the slab was divided into three sectors A, B and C, where the flow and border conditions are different; sector A is affected by the pouring of concrete, sector B has a high flow rate and is influenced by the lateral wall effect, and sector C is affected by the end of the formwork. Fig. 6 shows a scheme of the slab and the cut beams. The results of the shadowed beams will be used to verify the numerical model.

To evaluate the effects of fiber orientation, small beams 90 × 70 × 320 mm from different zones of the slab and with different orientation (directions parallel and normal to concrete flow) were cut. A notch depth of 15 mm and 300 mm span were used. Three-point bending tests were done following the general guidelines of EN 14651-2005 [55]. The load vs crack mouth opening displacement (CMOD) or relative displacement between both sides of the notch was recorded. As the load–CMOD response was determined on small beams, the same span/height and notch/height ratios as indicated in the standard were adopted, making possible to obtain the residual strength parameters [56]. The first crack stress (f_L), the maximum stress (f_M), and the residual strengths f_{R1}, f_{R2}, f_{R3}, f_{R4} were calculated.

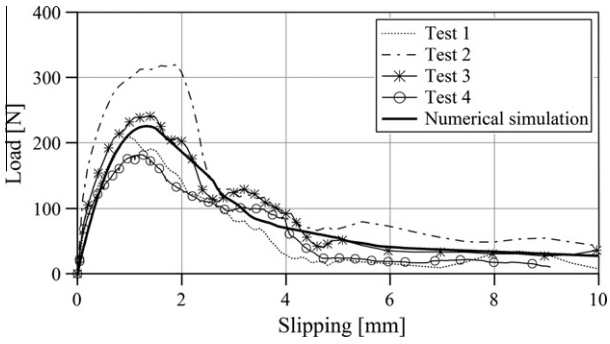

Fig. 5. Load–slipping curves obtained from the pull out tests of Fiber 5. Comparison of experimental and numerical results.

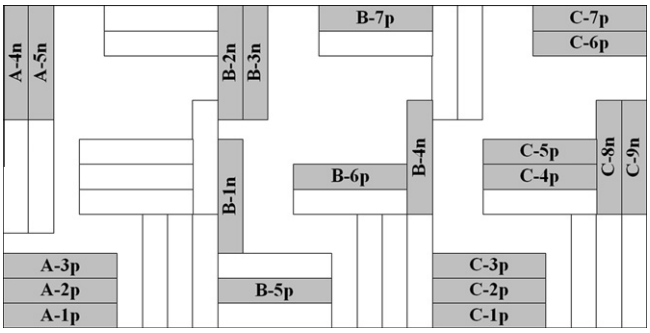

Fig. 6. Scheme of the slab and the cut beams.

Table 2
Summary of bending test results.

Stresses (MPa)	Sector A		Sector B		Sector C	
	Parallel	Normal	Parallel	Normal	Parallel	Normal
f_L	5.6	5.2	5.6	5.1	5.3	5.6
f_M	7.7	5.9	8.4	5.1	6.4	6.3
f_{R1}	4.7	2.8	5.2	1.7	3.6	3.0
f_{R2}	6.9	3.2	7.8	1.7	5.4	4.4
f_{R3}	7.5	3.2	8.3	1.8	5.9	5.1
f_{R4}	7.2	3.3	8.1	1.8	5.6	5.3
Mean fiber density on fracture surfaces (fibers/cm^2)						
	1.20	0.74	1.59	0.53	1.03	1.08

After bending tests, the density of fibers was determined on the fracture surfaces. The mean values corresponding to each zone are presented in Table 2. In addition, on the specimens chosen to verify the model, cuts were performed in the three directions obtaining the density of fibers in each plane.

3.2.2. Results

Fig. 7 shows typical load–CMOD curves of specimens cut from the slab differentiated by group and beam orientation with respect to the flow direction (parallel or perpendicular). A summary of the strength parameters is presented in Table 2; the mean values of all specimens from each sector and direction are given.

Table 1
Fibers dimensions and average results of pull-out tests.

Fiber	Scheme	f_y (MPa)	∅ (mm)	L (mm)	$L/\varnothing$	P_{peak} (N)	δ_{peak} (mm)	P_{resid} (N)	P_{peak}/V (N/mm^3)
1		1100	1.10	50	45.0	487	1.00	130	10.2
2		860	1.00	50	50.0	388	0.60	134	9.9
3		1100	0.75	50	67.0	333	0.70	96	15.1
4		2470	0.71	60	84.5	510	2.00	118	21.5
5		2470	0.45	35	77.7	230	1.30	25	41.9

0 10 20 30 40 50 60 [mm]

f_y: yield stress; Ø: diameter; L: length; P_{peak}: peak pull-out load; δ_{peak}: displacement corresponding to peak pull-out load; P_{resid}: load corresponding to 10 mm displacement; V: fiber volume.

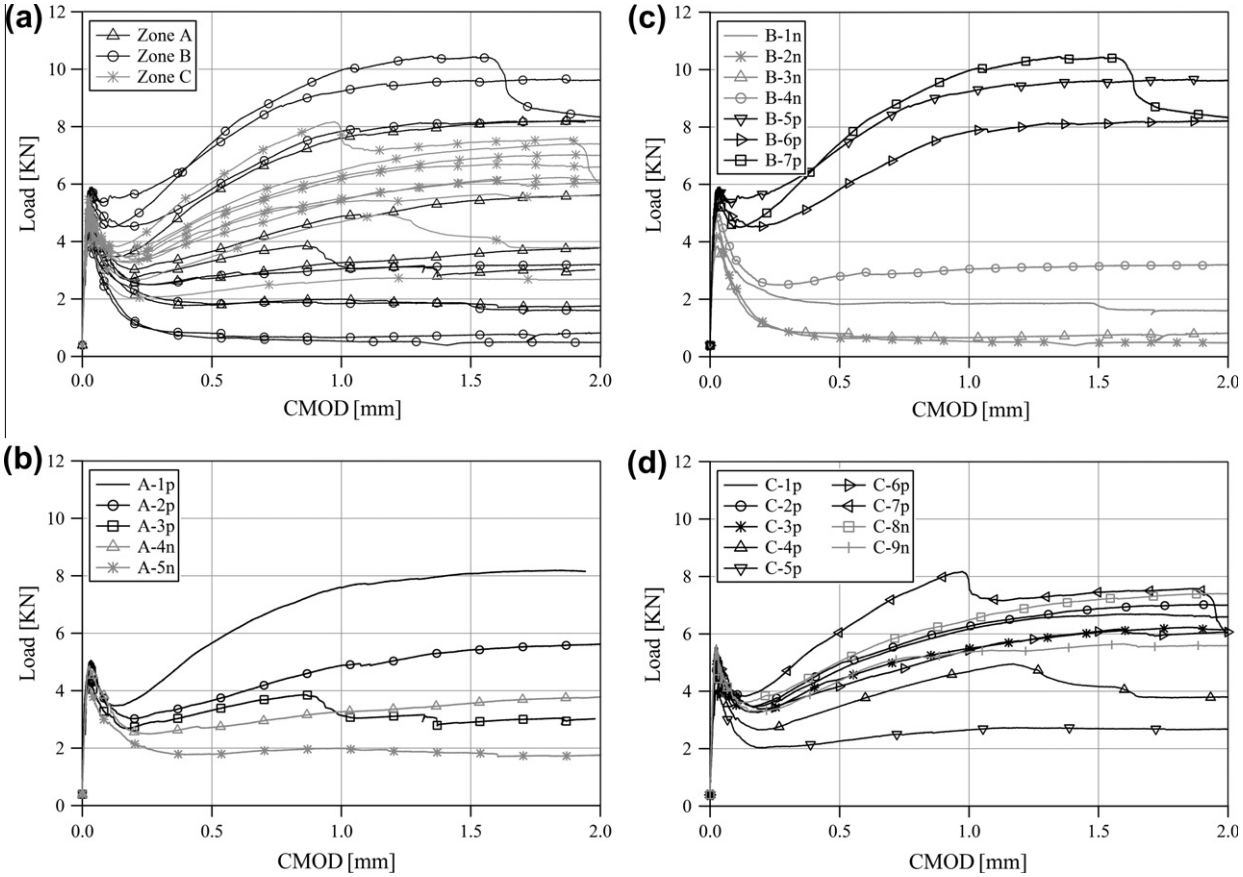

Fig. 7. Load–CMOD curves of specimens cut from the slab. (a) All beams, (b) zone A, (c) zone B, and (d) zone C.

It can be seen that f_L is similar in all sectors, as this parameter mainly depends on the matrix strength and it is less affected by the fiber orientation (Table 2). On the contrary, the post peak parameters show differences between each sector and beam orientation; these changes in the residual parameters are significant and should be considered for the structural design. The highest mean value of the maximum stress (f_M) and the residual strengths f_{R1}, f_{R2}, f_{R3}, f_{R4} correspond to the parallel beams of sector B followed by sector A.

Fig. 7 clearly shows variable post peak behaviors along the slab. Parallel beams have a higher postpeak residual capacity than normal beams, as fibers are orientated due to concrete flow; the unique exception is normal beam C-9n that is at the end of the mold. In addition parallel beams closer to the formwork walls show a better response than their companion internal beams (B-7p and B-5p > B-6p; C-1p and C-6p > C-4p); this is attributed to a better fiber alignment. When comparing sectors A, B, and C, it seems that the higher post peak parameters correspond to sector B followed by sector A, and finally sector C. The greater differences in the beam responses correspond to sector B, where the highest rate of flow combined with the wall effect enhance fiber orientation. In sector C due to the decrease in concrete velocity and the influence of the end of the formwork the fibers are less oriented.

Summarizing, there is a clear orientation of fibers, especially along the sector B where the differences between parallel and perpendicular beams are greater. In sector C the end of the formwork and the low flow rate reduces the orientation of the reinforcement leading to a more homogenous mechanical response.

These results show that there can be a great variation in the mechanical behavior when different zones of a structural element are considered. In this sense the possibility of modeling the effect of fibers orientation becomes relevant regarding SFRC applications.

4. Numerical simulation of SFRC tension response

4.1. Pull out response

The mean compression strength and the elasticity modulus were determined from standard characterization tests and are presented in Table 3. The rest of the matrix parameters used in the pull-out numerical model are independent of the fiber types and were obtained from calibration with the results of the 63 pull out tests previously described. The matrix parameters obtained are presented in Table 4.

Table 3
Concrete properties.

Elasticity modulus, E (MPa)	40200
Poisson ratio, ν	0.2
Uniaxial tension strength, σ_{ut} (MPa)	2.93
Uniaxial compression strength, σ_{uc} (MPa)	62.9
Uniaxial compression yield threshold, σ_{fc} (MPa)	44.0
Compression/tension elastic limit ratio, R^{0p}	15.0
Yield function	Modified Lubliner–Oller [27]
Compression equibiaxial/uniaxial ratio, Rbc	1.16
Parameter to control the shape of yield function in the Octahedric plane [27] γ	3.5
Tension hardening curve	Exponential
Compression hardening curve	Exponential maximum
Value of the plastic hardening variable for the peak compression stress, κ^p_{comp}	0.15
Fracture energy density, G^p_f (kN/mm)	0.029
Crush energy density, G^p_c (kN/mm)	3.6
Plastic potential function	Modified Lubliner–Oller [27]

The numerical pull-out curve obtained with the model described in Section 2.2.2 is compared in Fig. 5 with the experimental results. A good agreement is achieved.

4.2. SFRC tension response

The model described can be used to simulate the tension response of SFRC. This response mainly depends on the number of

Table 4
Matrix parameters for numerical simulation of pullout tests.

Compression strength (MPa)	62.9
Friction shear stress (MPa)	2.0
Friction coefficient	0.50

fiber crossing the transverse section and on the fiber properties. The curves obtained can be used to simulate SFRC as a concrete with a modified tension response avoiding the use of the composite model described for the simulation of structural problems.

Unfortunately no tension tests were performed for the concrete and fibers under study. Therefore, the results presented are only numerical and are later used for concrete as previously described and compared with experimental results from flexure tests.

The concrete tension behavior used for the slab for different number of fibers per unit of area is obtained in this section.

The properties used for concrete are those presented in Table 3. Some of them were obtained from compression and flexure tests while standard values were used for the rest [27].

The pull out curve of the fibers is the mean of experimental curves or that numerically obtained to reproduce this mean response. The fiber content in axial and transverse directions (Table 5) is taken into account in the numerical simulation.

Table 5
Beams dimensions and fiber content.

Beam	b (mm)	H (mm)	h_t (mm)	Fiber content (mm^2/mm^2)	
				k_x	k_y
C-1p	79	74	88	0.00185	0.00008
B-1n	78	73	89	0.00045	0.00059
A-4n	78	73	92	0.00103	0.00151
C-7p	76	77	91	0.00141	0.00132
C-4p	83	75	90	0.00130	0.00116
B-2n	76	75	94	0.00059	0.00049
C-9n	74	75	89	0.00186	0.00073
A-1p	79	70	80	0.00164	0.00132

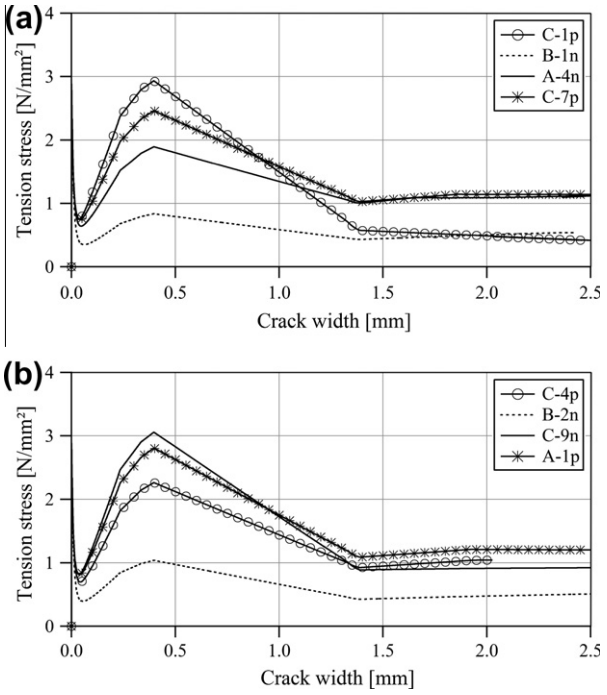

Fig. 8. Numerical simulation of SFRC tension response for different fibers contents. Stress vs crack width. (a) C-1p, B-1n, A-4n, C-7p; and (b) C-4p, B-2n, C-9n, A-1p.

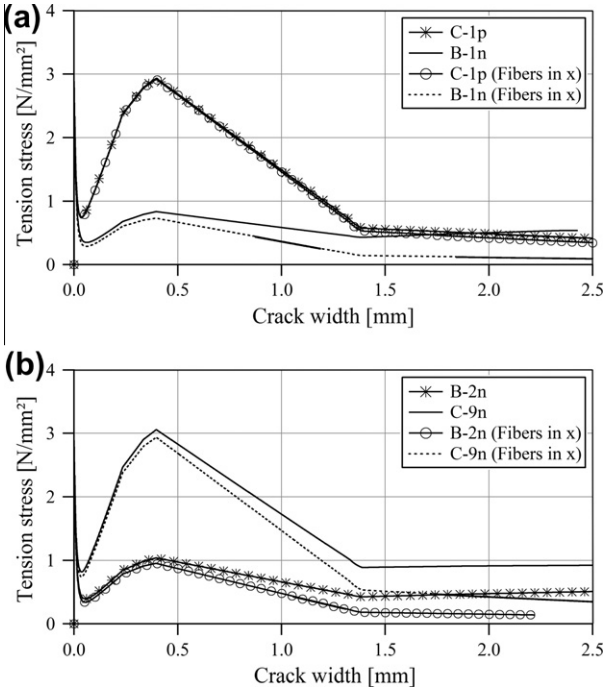

Fig. 9. Contribution of fibers in transverse direction. (a) C-1p, B-1n; and (b) B-2n, C-9n.

The results obtained for different fibers densities covering the range measured in the fracture plane of the beams extracted from the slab are presented in Fig. 8a and b. It is clear the effect of fiber density on tension response. Although the tensile strength is only slightly incremented the shape of the load–crack width curve and thus ductility strongly depend on the SFRC fiber content.

Fig. 9 shows the difference found in tension response of SFRC if only the axial content of fibers is taken into account. It is clear that when fiber content in transverse direction is not negligible, their contribution to tension response should be taken into account.

5. Numerical simulation of the beams tested under flexure

The numerical simulation of the flexure tests of the SFRC notched beams extracted from slab described in Section 3.2 is presented in this section. Different approaches previously described are used to model SFRC and are compared with experimental results corresponding to the same concrete matrix but different fibers orientations resulting from the SFRC slab casting process.

In all cases SFRC is modeled as a composite material formed by a concrete matrix with fibers distributed in three orthogonal directions in coincidence with beams principal symmetry axis. Different approaches are used to obtain the fibers pull-out response. Fiber debonding–slipping is:

(a) obtained from pull-out tests,
(b) obtained from numerical simulation, and
(c) approximated from one of the flexure tests results.

Approaches a and b give the same results because the numerical simulation of fiber debonding–slipping was calibrated to reproduce the results of pull out tests available.

5.1. Numerical model

The dimensions of the beams tested are slightly different and are presented in Table 5 and indicated in Fig. 10a. All the beams

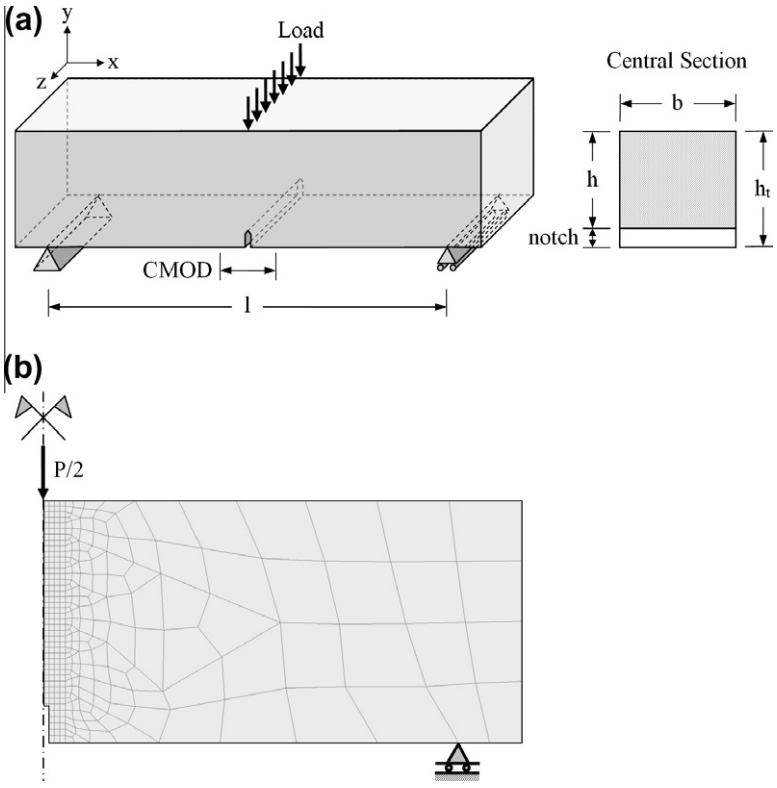

Fig. 10. Notched beams tested under flexure. (a) Beam's dimensions, and (b) finite element mesh.

have the same span (l = 300 mm). The fiber densities in planes *yz* and *xz* (k_x, k_y), obtained as the number of fibers per unit area by the fiber area are also included in Table 5.

The finite element mesh, load and boundary conditions used for the numerical simulation of the beams tested under flexure are presented in Fig. 10b. Taking advantage of the problem symmetry conditions, only one half of the beam was modeled. Four nodes isoparametric plane stress elements were used.

The finite element mesh used was chosen after proving mesh size independence of global structural response that is partly assured by the model used. The mesh was refined until no difference between two consecutive refinements was obtained. The effect of the type of finite elements used was also studied. As expected, quadrangular elements give a better description of the problem than triangular elements. The use of higher order quadrangular elements (with more than four nodes) is not expected to change the results for the mesh refinement used in this paper. There is still some almost negligible mesh size dependence that cannot be avoided and that was also pointed out by Belletti et al. [15]. This spurious mesh size dependence is related to the vertical finite element size. Cracking begins at the lowest integration points. As the mesh is refined these points are more distant from the neutral axis and more tensioned so cracking begins for lower loads. On the other side, only the higher integration points are in compression and thus a greater ultimate flexure moment (load) is obtained when a finer mesh is used.

5.2. Comparison of numerical and experimental results

The mechanical properties of concrete were partly obtained from standard characterization tests and partly estimated following the suggestions in Luccioni and Rougier [27]. Normally, the number of parameters of a constitutive model increases with its applicability to different materials and its ability to simulate more complex behavior and thus more tests are required to completely characterize material response. Nevertheless, if the model is to be applied to a material that is well known and broadly studied as steel or concrete, a good estimation of some of the parameters, for example as a function of compression strength as illustrated in Ref. [27], can be used to avoid performing many experimental tests. Although not always explicit, this procedure is vastly used in constitutive modeling when some functions or constants are a priori fixed.

The material parameters used in the numerical model are presented in Tables 1, 3 and 4.

The fibers contents in the direction of the beams symmetry principal axis and orthogonal to it are included in Table 5.

The fiber debonding–slipping curve was experimentally obtained from pull-out tests described in Section 3.1 and was also numerically modeled (see Section 2.2.2). The curves presented in Fig. 5 were used as input data defining the fiber hardening/softening behavior in approaches (a) (experimental curves) and (b) (numerical curve). In case of approach (c), the fiber debonding–slipping curve was indirectly obtained from the calibration of the flexure response of beam C-1p (Fig. 11) and then applied to the numerical simulation of the other beams.

Figs. 11–18 show the results obtained from the numerical simulation (approaches (a), (b) and (c)) of the beams tested and their comparison with experimental results. A reasonable agreement of numerical and experimental results is obtained in most cases. Comparing Figs. 11–18 with Fig. 7, it is observed that the numerical curves lie among experimental results for each zone in the slab that present an appreciable variability. The greater differences between numerical and experimental results are obtained for the groups of beams (A-4n, A-5n) and (B-2n-B-3n) that are located near the laterals of the framework and normal to concrete pouring direction (See Fig. 6). SFRC is an heterogeneous material with non-uniform spatial distribution of components. The fibers densities in

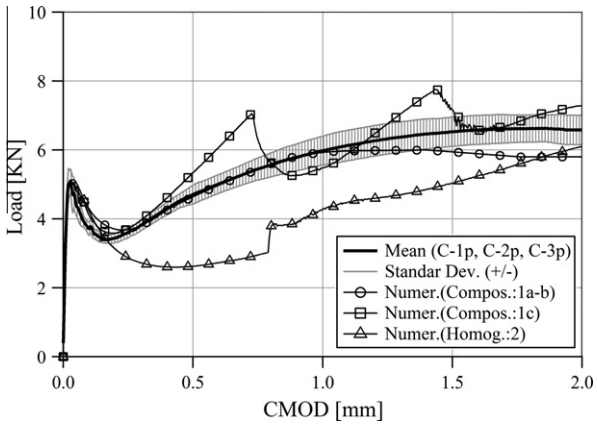

Fig. 11. Beams C-1p, C-2p, C-3p – comparison of numerical and experimental results.

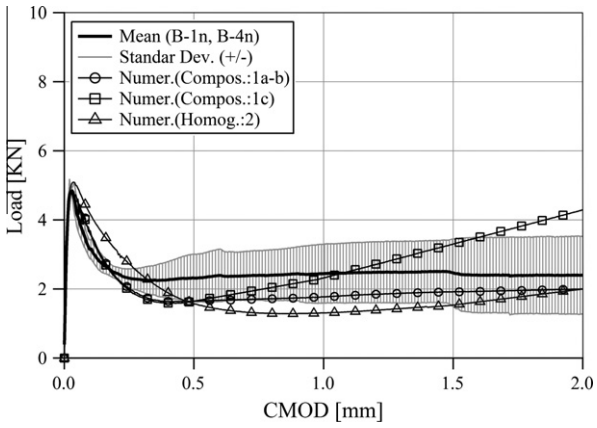

Fig. 12. Beams B-1n, B-4n – comparison of numerical and experimental results.

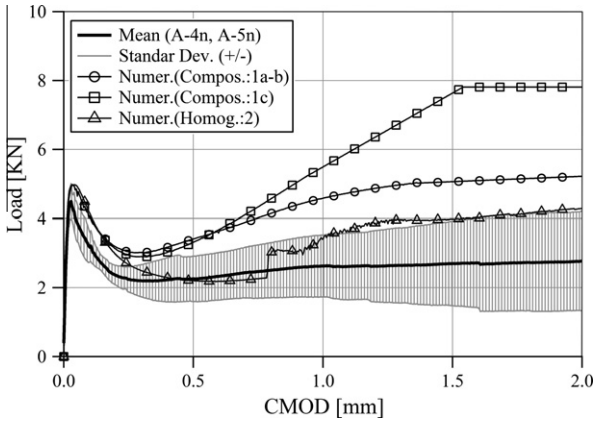

Fig. 13. Beams A-4n, A-5n – comparison of numerical and experimental results.

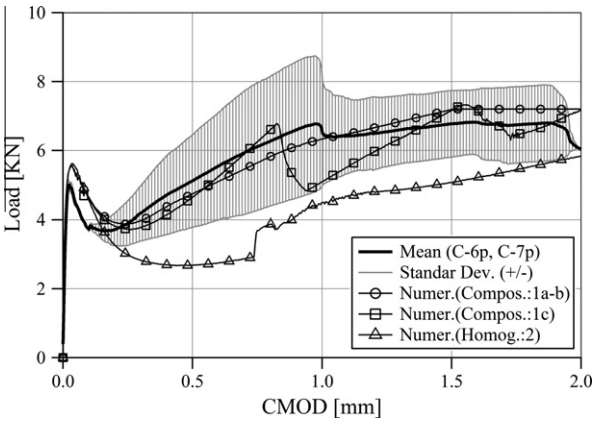

Fig. 14. Beams C-6p, C-7p – comparison of numerical and experimental results.

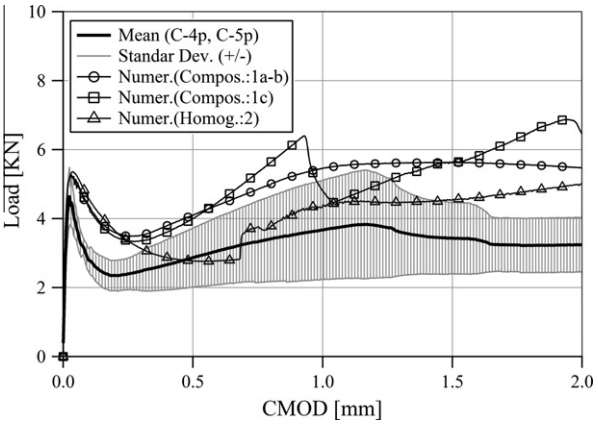

Fig. 15. Beam C-4p, C-5p – comparison of numerical and experimental results.

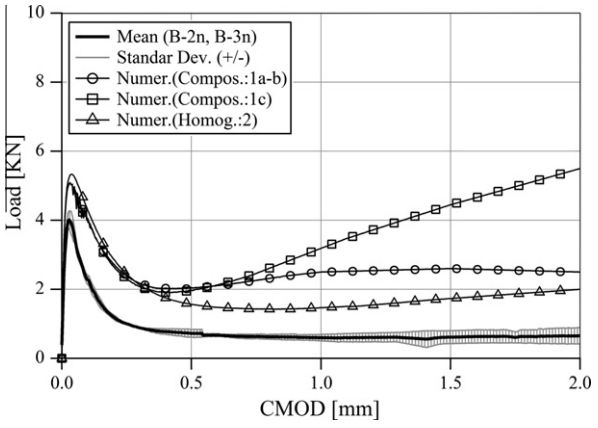

Fig. 16. Beam B-2n, B-3n – comparison of numerical and experimental results.

different directions were obtained from only one cut of each beam and were assumed uniform all over each beam in the numerical simulation. This simplification could be partly responsible for the differences observed between numerical and experimental results. Nevertheless, it should be observed that the differences are in the order of the differences obtained in the tests. Even for beams extracted from the same zone of the slab the experimental load–displacement curves present considerable differences among them. See, for example, the curves corresponding to beams A-1p, A-2p and A-3p in Fig. 7b.

The mean and the standard deviation of experimental results for groups of beams from the same zones were calculated. The results are included in Figs. 11–18 where the curves corresponding to the mean of experimental results for the zone is plotted and the area between the mean minus standard deviation and the mean plus standard deviation is shaded. It can be seen that except for the beams located near the laterals or the end of the framework the numerical curve corresponding to approaches (a) and (b) lies inside or near the shaded area.

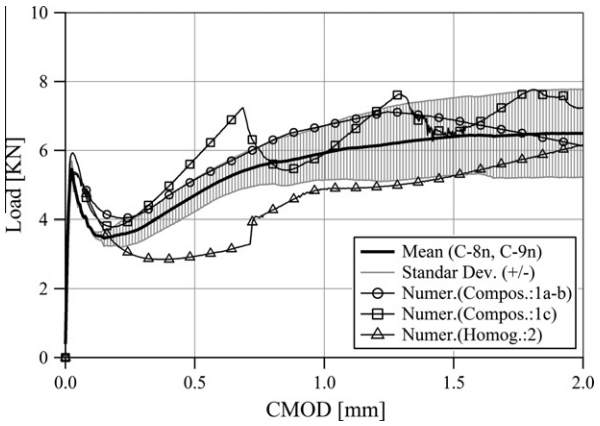

Fig. 17. Beam C-8n, C-9n – comparison of numerical and experimental results.

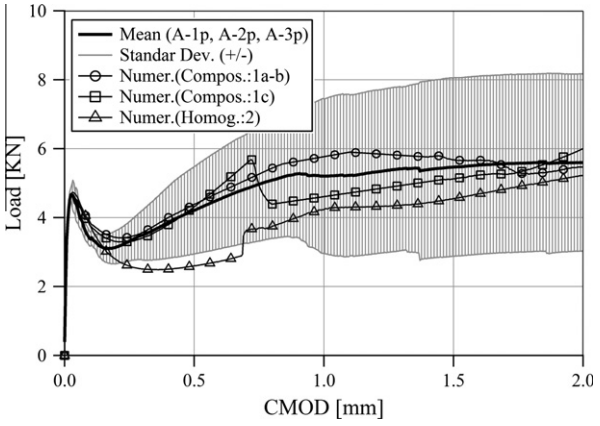

Fig. 18. Beam A-1p, A-2p, A-3p – comparison of numerical and experimental results.

The numerical results obtained with approach (c) are also included in Figs. 11–18. These results were obtained calibrating a bi-linear curve for the fibers pull-out curve in order to fit the flexure response of beam C-1p in Fig. 11. Then the curve was used to reproduce the experimental results of the rest of the beams (Figs. 11–18). Although the results are similar to those obtained with approaches (a) and (b), it is observed that indirectly obtaining the fibers pull-out curve from flexure results is somewhat cumbersome and can lead to some erroneous results when the response used corresponds to a distribution of fibers not only in axial direction. Moreover, as only the initial slope of the pull-out curve was calibrated, numerical results depart from experimental results when the crack width increases.

The wave phenomenon observed in numerical results from approach c is typical of the tension response of concrete and hardening fibers working with the strain compatibility assumption (Eq. (1)). In this case the composite stress is obtained as the sum of the contributions of concrete and steel fibers multiplied by their volume ratio (Eq. (5)). When fibers are in hardening regime, concrete is softening until it completely looses strength and the fibers are responsible of resisting the applied stress showing a hardening response. Depending on the material properties and the fibers volume fraction, the combination of these effects leads to a peak in stress followed by a strength loss and then a second hardening regime. In the case of flexure more than one local peak is numerically obtained as concrete cracking spreads upwards with the increase of applied displacement, involving more elements.

This phenomenon also takes place in the tests and sometimes it is evidenced in uniaxial tension experimental curves. Nevertheless, the physical flexure problem is a continuous problem where cracking advance is progressive and thus the waves are not marked as in numerical discrete approach (finite element) used to approximate the problem.

5.3. Comparison with numerical results obtained for an equivalent homogeneous material

The numerical results obtained in previous section are compared with those obtained modeling SFRC as an equivalent homogeneous material. For that purpose SFRC is modeled as a homogeneous elastoplastic material using the concrete model described in Section 2.1. This model requires the definition of the functions $\sigma_t(\kappa^p)$ and $\sigma_c(\kappa^p)$ used in Eq. (12). These functions can be directly obtained from the stress–strain curves in tension and compression respectively, with the aid of the plastic hardening variable definition (Eqs. (8)–(11)). Assuming that fiber addition has not influence on concrete behavior in compression, the stress–strain curve of plain concrete is used for SFRC in compression. As there were not experimental results for tension response, stress–strain curve in tension is obtained from a previous numerical simulation using the composite model described in Section 3 with fiber debonding–slipping behavior obtained from tests. The curves defining SFRC behavior in tension for different fiber contents are those previously presented in Fig. 8a and b.

The flexure response of the beams obtained with the homogeneous model for SFRC is shown in Figs. 11–18 and compared with experimental results and numerical results obtained modeling SFRC as composite material. It is observed that better agreement between experimental results is obtained when SFRC is simulated as a composite material since the effect of fibers in different directions can be approximated more accurately than in the case of an equivalent homogeneous isotropic model calibrated in one direction.

6. Conclusions

Experimental results from pull-out and flexure tests of SFRC present a great dispersion that in case of flexure tests can be attributed to the non-uniform distribution and orientation of fibers in concrete resulting from many factors, mainly related to the concrete casting process. The variability of the fiber contents measured in beams extracted from the slab and the consequent difference observed in their flexure response is a clear evidence of this observation.

In spite of this variability, predicting models are still necessary for design purposes. Among different types of models available in the literature, micro-mechanics based models have the advantage that they can explicitly take into account all the variables contributing to the differences observed. On the other side, macro-mechanics based models are more practical for design and analysis.

The model presented in this paper represents an attractive alternative to model SFRC since it incorporates information from the micro-scale in a very simple way. The composite model originally developed in Ref. [28] for long fibers reinforced composite was extended to model SFRC, a hooked end short fiber reinforced composite with fibers in different orientations. For this purpose, the model developed in Ref. [27] was used to simulate the concrete matrix while a further development of the pull out model presented in Ref. [51] combined with the anisotropy treatment described in Ref. [38] was used for the fibers.

The proposed model is able to reproduce fiber pull-out, tensile and flexure behavior of SFRC specimens with different fiber contents.

The proposed model is able to simulate the crack-opening flexure response of self-compacting steel fiber reinforced concrete beams with different fibers contents and distributions.

Different approaches to use the same model have been proposed and compared. The results show that fibers pull-out response and fibers content have an important influence on tensile behavior of SRFC. Although the tensile strength of SFRC is nearly the same than that of concrete, the shape of the tensile response curve strongly depends on fibers content and bond–slip behavior. If the fiber content orthogonal to tensile behavior is not negligible it has some influence in tensile response. This type of effects cannot be taken into account by equivalent homogeneous models mainly calibrated in tension because they assume an isotropic behavior based on experimental results calibrated for one direction.

As a consequence of the preceding observation flexure response is also strongly influenced by fiber content and bond–slip behavior. Fiber distribution can be approximately modeled as fibers in three orthogonal directions with different contents in each direction. While volumetric ratios are usually used for components in mixture theory, area ratios in three orthogonal planes are more adequate for this type of inclusion due to the geometry of the fibers. The effect of non-axial fibers in flexural response is not negligible. It is shown that numerical simulation of SFRC in bending with a calibrated tensile response can conduct to some errors in the residual strength that can be attributed to this cause. Conversely, it can be concluded that calibration of tension response of SFRC from flexure response can lead to some errors related to fiber content in non-axial directions.

Although the proposed model allows placing the fibers in any direction, the bond slip behavior has only been modeled for the case of fibers pulled out normally to concrete crack. This limitation has proved not to be important to model flexure response. Nevertheless, the model should be improved taking into account fiber inclination with respect to the crack plane in order to be able to reproduce more complicated stress states.

Acknowledgements

The authors wish to thank the financial support of National Agency for Scientific and Technological Promotion, National Scientific and Technological Research Council (CONICET) and National University of Tucumán research Council (CIUNT) and Ms Amelia Campos for the English revision.

References

[1] Grünewald S. Performance-based design of self-compacting fibre reinforced concrete. Ph.D. Thesis. Delft University of Technology; 2004.
[2] Stähli P, van Mier JGM. Manufacturing, fibre anisotropy and fracture of hybrid fibre concrete. Eng Fract Mech 2007;74:223–42.
[3] Vandewalle L, Heirman G, Rickstal FV. Fibre orientation in self-compacting fibre reinforced concrete. In: Gettu R, editor. Proceedings of 7th international RILEM symposium on fiber reinforced concrete. BEFIB 2008 India: Chennai. vol. 60. RILEM PRO; 2008. p. 719–28.
[4] Torrijos MC, Barragán B, Zerbino R. Placing conditions, mesostructural characteristics and post-cracking response of fibre reinforced self-compacting concretes. Constr Build Mater 2010;24:1078–85.
[5] Pasa Dutra VF, Maghous S, Campos Filho A, Pacheco AR. A micromechanical approach to elastic and viscoelastic properties of fiber reinforced concrete. Cem Concr Res 2010;40:460–72.
[6] Liu H, Xiang T, Zhao R. Research on non-linear structural behaviors of prestressed concrete beams made of high strength and steel fiber reinforced concretes. Constr Build Mater 2009;23:85–95.
[7] Barros J, Gettu R, Barragán B. Material nonlinear analysis of steel fibre reinforced concrete beams failing in shear. In: Sixth RILEM symposium on fibre reinforced concrete (FRC) BEFIB 2004. Varenna, Italy. vol. 39. RILEM PRO; 2004. p. 711–20.
[8] Mehmet Özcan D, Bayraktar A, Sahin A, Haktanir T, Türker T. Experimental and finite element analysis on the steel fiber-reinforced concrete (SFRC) beams ultimate behavior. Constr Build Mater 2009;23:1064–77.
[9] Peng X, Meyer C. A continuum damage mechanics model for concrete reinforced with randomly distributed short fibers. Comput Struct 2000;78:505–15.
[10] Wang ZL, Liu Y, Shen RF. Stress–strain relationship of steel fiber-reinforced concrete under dynamic compression. Constr Build Mater 2008;22:811–9.
[11] Campione G, Mangiavillano ML. Fibrous reinforced concrete beams in flexure: experimental investigation, analytical modelling and design considerations. Eng Struct 2008;30:2970–80.
[12] Wang ZL, Wub J, Wang JG. Experimental and numerical analysis on effect of fibre aspect ratio on mechanical properties of SRFC. Constr Build Mater 2010;24:559–65.
[13] Farnam Y, Mohammadi S, Mohammad S. Experimental and numerical investigations of low velocity impact behavior of high-performance fiber-reinforced cement based composite. Int J Impact Eng 2010;37:220–9.
[14] Antunes J, Gettu R, Kitsutaka Y. Inverse analysis procedures for determining the tensile stress–crack opening curve of concrete. RILEM TC 187-SOC 2007:31–41.
[15] Belletti B, Hendrix M, Rots J. Finite element modelling of FRC structures-pitfalls and how to avoid them. In: Gettu R, editor. Proceedings of 7th international RILEM symposium on fiber reinforced concrete. BEFIB 2008 India, Chennai. vol. 60. RILEM PRO; 2008. p. 303–13.
[16] Li VC, Wang Y, Backers S. Short random fiber reinforced brittle matrix composites. J Mech Phys Solids 1991;39(5):607–25.
[17] Geng YP, Leung CKY. Micromechanics-based fem simulation of fiber-reinforced cementitious composite components. Comput Struct 1997;64(516):973–82.
[18] Leung CKY, Geng YP. Micromechanical modeling of softening behavior in steel fiber reinforced cementitious composites. Int J Solids Struct 1998;35:4205–22.
[19] Lange-Kornbak D, Karihaloo BL. Tension softening of fibre-reinforced. Cementitious composites. Cement Concr Compos 1997;19:315–28.
[20] Li F, Li Z. Continuum damage mechanics based modelling of fiber reinforced concrete in tension. Int J Solids Struct 2001;38:777–93.
[21] Park K, Paulino GH, Roesler J. Cohesive fracture model for functionally graded fiber reinforced concrete. Cem Concr Res 2010;40:956–65.
[22] Gal E, Kryvoruk R. Meso-scale analysis of FRC using a two-step homogenization approach. Comput Struct. 2011;89(11–12):921–9.
[23] Bolander J. Numerical modeling of fiber-reinforced cement composites: linking material scales. In: Sixth RILEM symposium on fibre reinforced concrete (FRC) BEFIB 2004 Varenna, Italy. vol. 39, RILEM PRO; 2004. p. 45–60.
[24] Radtke FKF, Simone A, Sluys LJ. A computational model for failure analysis of fibre reinforced concrete with discrete treatment of fibres. Eng Fract Mech 2010;77:597–620.
[25] Cunha VMCF, Barros JAO, Sena-Cruz JM. An integrated approach for modelling the tensile behaviour of steel fibre reinforced self-compacting concrete. Cem Concr Res 2011;41:64–76.
[26] Luccioni B, Oller S, Danesi R. Coupled plastic-damaged model for concrete. Comput Methods Appl Mech Eng 1996;129:81–9.
[27] Luccioni B, Rougier V. A plastic damage approach for confined concrete. Comput Struct 2005;83:2238–56.
[28] Luccioni B, López D, Danesi R. Bond slip in reinforced concrete elements. ASCE's J Struct Eng 2005;131(11):1690–8.
[29] Naaman AE, Namur G, Alwan Jamil M, Najm Husam S. Fiber pullout and bond slip. II: experimental validation. J Struct Eng 1991;117(9):2791–800.
[30] Naaman AE, Bentur A, Wu ST, Banthia N, Baggott R, Hansen W, et al. Fiber–matrix interfaces. High Perform Fiber Reinf Cem Compos (HPFRCC2) 1996:149–92.
[31] Naaman AE. Engineered steel fibers with optimal properties for reinforcement of cement composites. J Adv Concr Technol 2003;1(3):241–52.
[32] Chanvillard G. Modelling the pullout of wire-draw steel fibers. Cem Concr Res 1999;29:1027–37.
[33] Luccioni B. Constitutive model for fibre reinforced composite laminates. J Appl Mech 2006;73(6):901–10.
[34] Toledo M, Nallim L, Luccioni B. A micro–macromechanical approach for composite laminates. Mech Mater 2008;40:885–906.
[35] Truesdell C, Toupin R. The classical field theories. In: Flugge S, editor, Handbuch der Physik II/I. Berlin: Springer; 1960.
[36] Maugin GA. The thermomechanics of plasticity and fracture. Cambridge, UK: Cambridge University Press; 1992.
[37] Betten J. Application of tensor functions to the formulation of yield criteria for anisotropic materials. Int J Plast 1988;4:29–46.
[38] Luccioni B, Oller S, Danesi R. Plastic damaged model for anisotropic materials. Appl Mech Am 1995;I:124–9.
[39] Oller S, Botello S, Miquel M, Oñate E. Anisotropic elasto-plastic model based on an isotropic formulation. Eng Comput 1995;12:245–62.
[40] Car E, Oller S, Oñate E. A large strain plasticity model for anisotropic composite material application. Int J Plast 1999;17(11):1437–63.
[41] Oller S, Car E, Lubliner J. Definition of a general implicit orthotropic yield criterion. Comput Method Appl Mech 2003;192:895–912.
[42] Alwan JM, Naaman AE, Hansen W. Pull-out work of steel fibers from cementitious composites: analytical investigation. Cem Concr Compos 1991;13(4):247–55.
[43] Bazant ZP, Li Z, Thoma M. Identification of stress–slip law for bar or fiber pull-out by size effect tests. J Eng Mech 1995;121(5):620–5.
[44] Alwan JM, Naaman AE, Guerrero P. Effect of mechanical clamping on the pull-out response of hooked steel fibers embedded in cementitious matrices. Concr Sci Eng 1999:15–25.

[45] Guerrero P, Naaman AE. Effect of mortar fineness and adhesive agents on pullout response of steel fibers. ACI Mater J 2000;97(1):12–20.
[46] Barragán BE, Gettu R, Martín MA, Zerbino R. Uniaxial tension test for steel fibre reinforced concrete-a parametric study. Cem Concr Compos 2002;25: 767–77.
[47] Robins P, Austin S, Jones P. Pull-out behaviour of hooked steel fibres. Mater Struct 2002;35:434–42.
[48] Sujivorakul C, Naaman AE. Modeling bond components of deformed steel fibers in FRC composites. High Perform Fiber Reinf Cem Compos (HPFRCC4) 2003:35–48.
[49] Cunha V, Sena-Cruz JM, Barros JAO. Impact of the fibre manufacturing quality on the fibre pullout performance. In: Gettu R, editor. Proceedings of 7th international RILEM symposium on fiber reinforced concrete. BEFIB 2008 India: Chennai. vol. 60. RILEM PRO; 2008. p. 83–93.
[50] Markovich I, van Mier JGM, Walraven JC. Single fiber pullout from hybrid fiber reinforced concrete. Microlab/Concr Struct, Delft University of Technology. HERON 2001; 46(3).
[51] Isla FA, Luccioni BM. Arrancamiento de fibras en hormigones reforzados con fibras. Mecánica Computacional 2009;28(26):2175–98.
[52] Naaman AE, Namur G, Alwan Jamil M, Najm Husam S. Fiber pullout and bond slip. I: analytical study. J Struct Eng 2001;117(9):2769–90.
[53] Ortiz M, Simo JC. An analysis of a new class of integration algorithms for elastoplastic constitutive relations. Int J Numer Methods Eng 1986;83: 353–66.
[54] Wang ZL, Wu J, Wang JG. Experimental and numerical analysis on effect of fiber aspect ratio on mechanical properties of SRFC. Constr Build Mater 2010;24:559–65.
[55] European standard EN 14651-05. Test method for metallic fibered concrete – measuring the flexural tensile strength (limit of proportionality (LOP), residual); 2005.
[56] Giaccio G, Tobes JM, Zerbino R. Use of small beams to obtain design parameters of fiber reinforced concrete. Cem Concr Compos 2008;30(4):297–306.